Mechanical Systems and Signal Processing 256 (2026) 114462

Contents lists available at ScienceDirect

Mechanical Systems and Signal Processing

journal homepage: www.elsevier.com/locate/ymssp

Full Length Article

Development of a camera-laser-IMU system for non-contact transverse displacement estimation using an adaptive extended Kalman filter

Mahsa Sanei [a], Piedad Miranda-Chiquito [a], G. Matthew Fricke [b], Fernando Moreu [a,*]

[a] Civil, Construction, and Environmental Engineering Department, University of New Mexico, Albuquerque, NM 87131, USA
[b] Department of Computer Science, University of New Mexico, Albuquerque, NM 87106, USA

ARTICLE INFO

Keywords:
Inertial measurement unit
Laser
Extended Kalman Filter
Data fusion
Dynamic displacement

ABSTRACT

Monitoring lateral displacement in railroad bridges is important because excessive displacements can increase derailment risk during train crossings. Traditional displacement measurement systems require invasive installations, posing safety and operational challenges. To overcome these limitations, this study developed a non-contact, sensor-fusion-based system that combines a laser, camera, and inertial measurement unit (IMU) through an Extended Kalman Filter (EKF), designed for future deployment on an Unmanned Aerial Vehicle (UAV). The EKF used in this study incorporates an innovation-based adaptive mechanism that dynamically adjusts process and measurement noise covariance, allowing the system to respond to changing sensor uncertainties during UAV-induced motion. A controlled indoor UAV flight was conducted under a motion capture system to inform the design of subsequent laboratory tests. Given the importance of UAV rotational motion for measurement accuracy, a six-degree-of-freedom (6DOF) platform was used to simulate UAV dynamics through combined translational and rotational movements. The system was evaluated under four motion scenarios. Estimated displacements were compared against two contact and non-contact ground truth measurements, as well as a previously developed camera-laser system by other researchers. The developed system outperformed the camera-laser method, reducing peak errors by 69.1% and Root-Mean-Square Error by 68.3%. The fusion approach was particularly effective under yaw-dominated motion. Correlation and phase-shift analyses showed that error magnitude increased when translational and rotational motion were misaligned, while phase-aligned conditions yielded the lowest average error. The current validation was performed in a controlled laboratory setting to evaluate the system and algorithm as a foundation for future field deployment.

1. Introduction

Many railroad bridges in the United States are aging and in need of repair or replacement. According to the ASCE report card, over 61,000 railroad bridges across the country are more than 100 years old [1]. The main issues with this infrastructure include structural

* Corresponding author at: Centennial Engineering Center 3051, 210 University Blvd, NE, MSC01 1070, Albuquerque, NM 87131, USA.
E-mail address: fmoreu@unm.edu (F. Moreu).

https://doi.org/10.1016/j.ymssp.2026.114462
Received 27 August 2025; Received in revised form 27 March 2026; Accepted 17 May 2026
Available online 26 May 2026

deterioration, outdated materials, and limitations in inspection and maintenance caused by budget constraints [2]. Accurate health monitoring of the railroad bridges is essential for maintaining the structural performance and ensuring safety due to the heavy dynamic loads imposed during train crossings. In recent years, advanced technologies have provided different solutions for more accurate and frequent railroad bridge health monitoring.

Transverse displacement, or the lateral, out-of-plane movement, is one of the important parameters used to track the health of railroad bridges. Excessive transverse displacement can show potential issues in the bridge's integrity, which, if unaddressed, could cause structural failure or derailment [3,4]. Railroad bridge monitoring has long relied on different sensor technologies to measure parameters like transverse displacement. Researchers and inspectors have employed devices such as accelerometers [5,6,7] and LVDTs [4] to measure bridge displacements. Accelerometers are advantageous because they can measure displacement without needing a fixed reference point. However, this method requires double integration of the data, which can cause inaccuracies, especially at lower frequencies [8]. Additionally, using an LVDT or an accelerometer requires direct access to the structure for sensor installation and typically depends on wired connections to transmit data. To address these challenges and improve operational safety, there is increasing interest among inspectors and railroad operators in using contact-free and reference-free inspection methods.

The use of wireless smart sensors, cameras, and UAVs as non-contact and reference-free methods for bridge monitoring has become popular in recent years. In earlier studies, wireless smart sensors were employed to monitor bridges but, like other sensors, they still require some level of access to the structures for installation [9,10,11]. The use of UAVs and cameras has created new opportunities for bridge inspections by enhancing accessibility and safety. Cameras are often preferred over contact-based sensors because they are more mobile, user-friendly, and make data collection easier. Many studies have used ground-based cameras for this purpose [12,13,14,15,16,17]. Most of them have focused mainly on tracking the vertical and in-plane displacement of bridges, often ignoring lateral displacements and changes in the camera's orientation. Additionally, many researchers have studied the use of a camera mounted on a UAV for the non-contact inspection of structures and bridges [18,19,20,21,22,23]. These studies mainly focused on providing visual or static information about the structures. Additionally, these approaches are limited by the low resolution of the camera, slow frame rates and a reduced ability to detect out-of-plane movements accurately. Nasimi et al. [24] improved this camera-based displacement approach by introducing a UAV-based system integrating laser and camera sensors to measure transverse displacement of a railroad bridge using a pinhole camera model. Their developed system was tested in indoor and outdoor with acceptable millimeter accuracy for railroad application; however, their proposed method was sensitive to excessive UAV motion which affected the measurement precision. Therefore, a new method is required to capture dynamic non-contact reference-free displacement data of bridge while accounting for UAV motion dynamics.

One solution to address the limitation of non-contact camera-based displacement estimation is to incorporate other sensors in the system that could help to capture UAV motion. Inertial sensors, such as accelerometers or gyroscopes, provide important information about the device's speed and acceleration [25]. Inertial sensors are especially useful in environments with limited visual signs, like featureless environments or in cases of rapid acceleration [26]. The Visual Inertial Odometry (VIO) is a technique in computer vision which is used to determine the position and direction of a device, like a camera or robot, by combining information from both visual sensors and inertial sensors such as IMU [27]. Cameras usually provide sufficient information in two images to estimate the rotational motion component and the translational motion component. However, because image formation is projective, the distance information is lost and the recovery is limited to translational direction minus magnitude [28]. So, the integration of camera and IMU enhances positioning performance by mutually complementing precision and frequency response [29]. Researchers have used sensor fusion techniques to estimate displacement of objects using camera and IMU. Meronen et al. [30] discussed a motion tracking system that fuses information from an IMU and a camera focusing on a visually dense approach using a learning-based optical flow model combined with conventional inertial navigation. Li et al. [31] proposed a system that achieves 3D motion tracking and high-quality reconstruction models in real time using camera and IMU sensors. Fang et al. [32] combined an IMU and a monocular camera in mobile devices to achieve real-time ego-motion by proposing a loosely coupled method in the error-state EKF framework. Hol et al. [33] fused the data of inertial and vision measurement using an EKF and a nonlinear state to estimate the real-time position of a camera. Angelio et al. estimated the UAV attitude integrating IMU, camera video and GPS using a linearized Kalman filter [34]. Zhang et al. proposed a method that combines monocular vision and IMU for indoor positioning, using different feature detection strategies for varied motion speeds [35]. Alatise et al. developed a system including IMU and camera to estimate the position of a mobile robot using an object detection algorithm, Speeded-Up Robust Features (SURF), combined with Random Sample Consensus (RANSAC) [36]. Poulose et al. evaluated different systems in an indoor environment and showed that combining IMU data with camera-based localization techniques, such as oriented fast rotated binary robust independent elementary features (BRIEF)-SLAM and UcoSLAM, leads to reduced localization errors [37]. Zhao et al. proposed using LiDAR-IMU-Camera for positioning and mapping estimation using Kalman filter. They used loop closure detection to enhance the accuracy of position estimation [38]. Wang et al. proposed a system that integrates monocular vision and IMU data using homography-based visual odometry and IMU measurements to estimate the motion of the helicopter with EKF in a GPS-denied environment [39]. Bednář et al. used camera for navigation system of the UAV; however, depending on the application and accuracy requirement, camera, IMU, or GPS can be used to get motion data from the UAV [40]. Ma et al. proposed a two-target method for in-plane and out-of-plane displacement estimation using monocular camera and accelerometer [41].

Several alternative non-contact displacement measurement approaches exist, each with distinct capabilities and limitations. Ground-based camera systems [12,13,14,15,16,17] have demonstrated sub-millimeter accuracy for in-plane displacement tracking but are fundamentally limited in measuring transverse (out-of-plane) displacement without a depth-sensing mechanism. UAV-mounted Laser Doppler Vibrometers [22,23] can measure along the beam direction with high precision but require expensive instrumentation and are sensitive to platform motion. Radar-based approaches, such as ground-based interferometric radar, offer long-range, all-

weather capabilities but measure displacement only along the radar line-of-sight, require stationary deployment, and involve significant cost and complexity [42,43]. The present work addresses the specific gap of millimeter-scale transverse displacement measurement from a moving platform using low-cost sensor components. Parallel advancements in adaptive mechanical hardware, such as the magnetic quasi-zero stiffness isolator in [44], further motivate the need for high-fidelity displacement sensing to enable closed-loop vibration control. Recent advances in spectral element methods for free vibration analysis of thin-walled structures [45,46], enable high-accuracy structural dynamic predictions. The experimental framework developed here complements these numerical approaches.

EKF-based sensor fusion is well established in robotics and navigation, however, its application depends on the measurement objective. Most camera–IMU fusion studies focus on ego-motion estimation for navigation, SLAM, or in-plane displacement tracking. In contrast, this study aims to estimate the displacement of an external structure from a moving platform, requiring separation of platform motion from structural motion. Transverse (out-of-plane) displacement is particularly challenging for vision systems because it produces subtle scale changes rather than clear pixel shifts, making laser ranging necessary for depth resolution. A key design choice is excluding the laser from the EKF: since the laser measures the combined effect of platform and structural motion, it cannot be used directly in the filter without a structural dynamics model, which would reduce generality. Instead, the EKF fuses only camera and IMU data to estimate platform motion, and the laser measurement is corrected afterward, enabling model-free, reference-free displacement estimation. The innovation-based adaptive estimation is tailored for moving platforms like UAVs, where camera noise can change abruptly due to motion blur while process dynamics evolve more gradually. To the authors' knowledge, no prior work demonstrates a UAV-borne fusion of IMU, camera, and laser specifically for millimeter-scale transverse bridge displacement. This study addresses that gap by coupling range- and image-based sensing with IMU-informed motion compensation within the previously developed NASIMI system using an innovation-adaptive EKF. The enhanced system, designed for UAV deployment, employs this filter to mitigate the camera's sensitivity to high-frequency motion and the IMU's long-term drift. To evaluate the influence of UAV-induced motion on displacement estimation accuracy, the study conducted controlled laboratory experiments using a 6DOF hexapod platform that simulated both translational and rotational UAV dynamics. Displacement results from the proposed IMU-camera-laser system were quantitatively compared with the original NASIMI approach [47] and with ground truth data obtained from high-precision sensors. This paper details the state-of-the-art for displacement estimation, methodology for sensor fusion and displacement correction, system hardware configuration, UAV indoor flight compared with selected 6DOF platform, experiment setup and description, a comprehensive analysis of experimental results across multiple motion scenarios, challenges and future work, and conclusion.

2. Methodology

The objective of this study is to measure the out-of-plane displacement of a simulated railroad bridge from a moving platform using a non-contact reference-free approach. The developed methodology is based on a method from Nasimi and Moreu [48], which uses a camera pinhole model [49] and bundle adjustment [50] to track displacement of a railroad bridge using a camera and laser mounted on a UAV. To evaluate the algorithm's performance under realistic motion conditions, a 6DOF Stewart platform (hexapod) [51] carrying multiple sensing devices was used to replicate UAV dynamics in a controlled laboratory setting. The key innovation in this

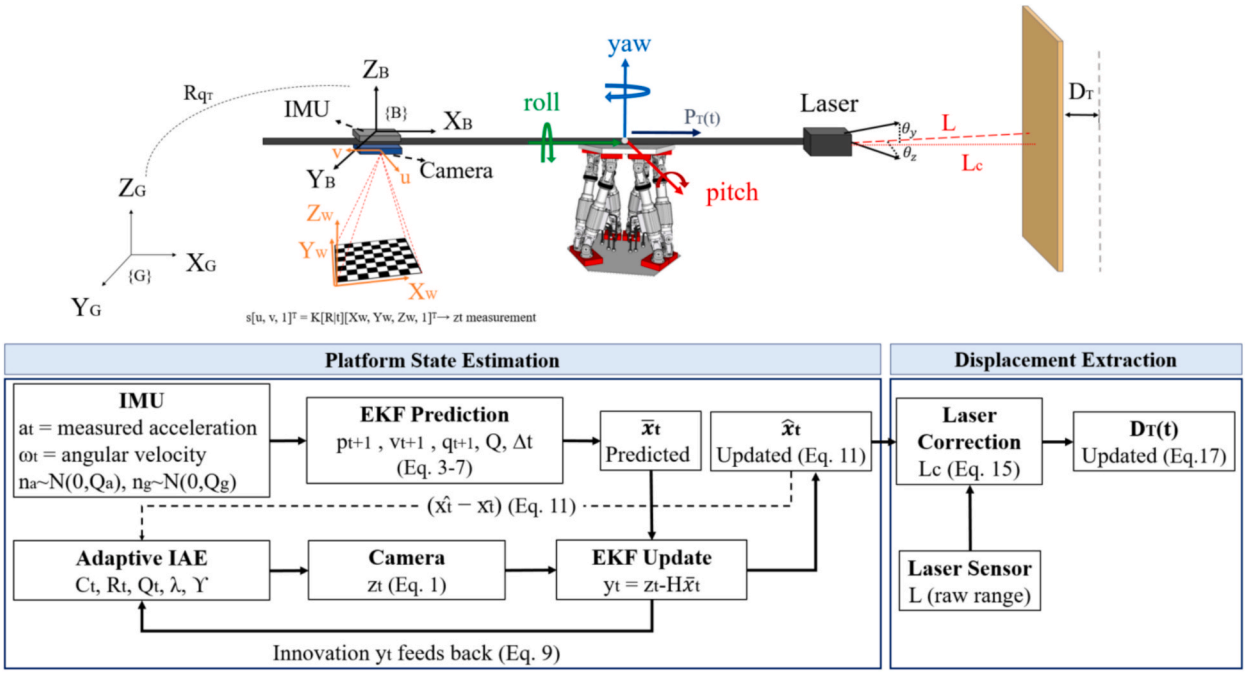

Fig. 1. Experiment measurement geometry and coordinate frames, Adaptive EKF data flow.

study is the addition of an IMU and fusing the IMU and camera data to enhance measurement accuracy due to IMU's ability to detect high-frequency vibrations and accurately track the UAV motion that would be difficult to capture using only camera and laser. Fig. 1 shows the measurement geometry and coordinate frames, and the adaptive EKF data flow of the experiment in this study.

2.1. Camera projection model

The system operates by using a camera mounted on a hexapod to track the platform's motion relative to a known checkerboard pattern using a calibrated pinhole projection model. The mapping between a 3D world point (X_w, Y_w,Z_w) and its 2D image coordinates (u, v) is given by equation (1).

$$s\begin{bmatrix} u \\ v \\ 1 \end{bmatrix} = \mathrm{K}[\mathrm{R} \quad \mathrm{t}]\begin{bmatrix} X_w \\ Y_w \\ Z_w \\ 1 \end{bmatrix} \tag{1}$$

where s is the scale factor, K is the intrinsic matrix obtained from camera calibration, and $[\mathrm{R} \quad \mathrm{t}]$ are the extrinsic rotation and translation parameters obtained from each camera frame using the known checkerboard geometry. The checkerboard provides known world coordinates (X_w, Y_w, Z_w) that enable the camera pose estimation, producing the measurement vector z_t containing estimated camera position and orientation used in the EKF update step.

2.2. EKF state vector and prediction

At the same time, IMU data (acceleration and gyroscope signals) are loaded, corrected for bias and gravity, and used to compute orientation, velocity, and position. The EKF framework begins with defining a state vector including position, velocity, orientation, and sensor biases that represents the physical and dynamic properties of the hexapod platform, accounting for both translational and rotational motion as well as systematic sensor errors. The state at time t is expressed in equation (2).

$$\mathrm{x}_t = \left[\mathrm{p}_t,\ \mathrm{v}_t,\ \mathrm{q}_t,\ \mathrm{b}_g, \mathrm{b}_a\right]^T \tag{2}$$

where $\mathrm{p}_t = \left[p_x, p_y, p_z\right]^T$ is the 3D position vector in the global coordinate frame {G}, $\mathrm{v}_t = \left[v_x, v_y, v_z\right]^T$ is the corresponding linear velocity, $\mathrm{q}_t = \left[q_w, q_x, q_y, q_z\right]^T$ is the orientation represented as a unit quaternion to avoid gimbal lock, $\mathrm{b}_g = \left[b_{g_x}, b_{g_y}, b_{g_z}\right]^T$ and $\mathrm{b}_a = \left[b_{a_x}, b_{a_y}, b_{a_z}\right]^T$ represent the gyroscope and accelerometer biases, respectively. Depending on whether the incoming event is from the camera or IMU, the EKF either performs a prediction step or an update step. In the prediction step, the IMU provides linear acceleration a_t and angular velocity ω_t, both expressed in the body frame {B}. These measurements are corrected by subtracting estimated biases. The position is updated using equation (3).

$$\mathrm{p}_{t+1} = \mathrm{p}_t + \mathrm{v}_t\Delta t + \frac{1}{2}\mathrm{R}(q_t)(\mathrm{a}_t - \mathrm{b}_a - \mathrm{n}_a)\Delta t^2 \tag{3}$$

Here, $\mathrm{R}(q_t)$ is the rotation matrix corresponding to the current orientation q_t, mapping vectors from the body frame {B} to the global frame {G}, and n_a $\mathcal{N}(0, Q_a)$ is the process noise associated with acceleration. The velocity update is computed using equation (4).

$$\mathrm{v}_{t+1} = \mathrm{v}_t + \mathrm{R}(q_t)(\mathrm{a}_t - \mathrm{b}_a - \mathrm{n}_a)\Delta t \tag{4}$$

Orientation is updated using quaternion multiplication and the exponential map, which converts angular velocity into a small rotation quaternion, as given by equation (5).

$$\mathrm{q}_{t+1} = \mathrm{q}_t \otimes \exp\left(\frac{1}{2}(\omega_t - \mathrm{b}_g - \mathrm{n}_g)\Delta t\right) \tag{5}$$

where $\otimes$ denotes the Hamilton quaternion product, and n_g $\mathcal{N}(0, Q_g)$ is the noise in angular velocity. For two quaternions $\mathrm{a} = [\mathrm{a_w}, \mathrm{a_x}, \mathrm{a_y}, \mathrm{a_z}]$ and $\mathrm{b} = [\mathrm{b_w}, \mathrm{b_x}, \mathrm{b_y}, \mathrm{b_z}]$, their product is defined in equation (6).

$$a \otimes \mathrm{b} = \begin{bmatrix} \mathrm{a_w b_w} - \mathrm{a_x b_x} - \mathrm{a_y b_y} - \mathrm{a_z b_z} \\ \mathrm{a_w b_x} + \mathrm{a_x b_w} + \mathrm{a_y b_z} - \mathrm{a_z b_y} \\ \mathrm{a_w b_y} - \mathrm{a_x b_z} + \mathrm{a_y b_w} + \mathrm{a_z b_x} \\ \mathrm{a_w b_z} + \mathrm{a_x b_y} - \mathrm{a_y b_x} + \mathrm{a_z b_w} \end{bmatrix} \tag{6}$$

The term $\exp(\tfrac{1}{2}\,\delta\theta)$ represents the quaternion exponential map, which converts a small rotation vector $\delta\theta = (\omega_t - \mathrm{b}_g - \mathrm{n}_g)\Delta t$ into a unit quaternion representing an incremental rotation over time Δt. For small angles, this is approximated as $\exp(\tfrac{1}{2}\,\delta\theta) \approx [1, \tfrac{1}{2}\,\delta\theta_x, \tfrac{1}{2}\,\delta\theta_y, \tfrac{1}{2}\,\delta\theta_z]$ followed by normalization to enforce the unit quaternion constraint. This first-order approximation is valid in this system because the IMU operates at 100 Hz and rotational velocities remain below $\pm\,20^\circ$/s, ensuring that the angular increment per time step is small. The result is normalized to enforce the unit quaternion constraint. Equation (7) presents the process noise covariance matrix incorporating uncertainty across all state components.

$$Q = \mathrm{diag}\left(Q_p, Q_v, Q_q, Q_g, Q_a\right) \tag{7}$$

The predicted state covariance is propagated as mentioned in equation (8).

$$\overline{P}_t = F_t P_{t-1} F_t{}^T + Q \tag{8}$$

where F_t is the Jacobian of the state transition model evaluated at the current state estimate.

2.3. EKF measurement update

The EKF computes the innovation (measurement residual) using equation (9), when a camera measurement z_t is received which provides the estimated 6-DOF camera pose.

$$y_t = z_t - H\overline{x}_t \tag{9}$$

where $\overline{x}_t$ is the predicted state, and H is the measurement model matrix that extracts the position and orientation components from the state vector to map it into the measurement space. The innovation y_t captures the discrepancy between expectation and observation, and so reflects what the model failed to predict. This "surprise" is the core signal used for updating both Q_t and $\mathrm{R_t}$ [52]. The Kalman gain is then computed using equation (10).

$$K_t = \overline{P}_t H^T \left(H\overline{P}_t H^T + R_t\right)^{-1} \tag{10}$$

The state estimate is corrected using the Kalman gain and the innovation stated in equation (11) and the state covariance is updated as stated in equation (12).

$$\widehat{x}_t = \overline{x}_t + K_t y_t \tag{11}$$

$$P_T = (I - K_t H)\overline{P}_t \tag{12}$$

where I is the identity matrix. These standard EKF update equations correct the predicted state using the camera-derived measurement, completing one filter cycle.

2.4. Innovation-based adaptive estimation (IAE)

IAE technique is integrated into the filtering framework to enhance the adaptability of the EKF under dynamic and uncertain measurement conditions. The goal is to adaptively tune the process and measurement noise covariances Q_t and R_t using recent sensor innovations, without relying on a large buffer of historical data. This ensures that the filter can self-tune in real time based on the evolving statistics of the system, without requiring offline calibration or fixed assumptions about noise characteristics. This adaptive behavior is driven by the system's innovation y_t (Eq. (9), which represents the new information provided by incoming measurements. This study uses a forgetting factor approach to recursively estimate the innovation covariance [53] rather than averaging past innovations over a sliding window. The empirical innovation covariance C_t [54] tracks the observed statistical spread of the innovation sequence over time. It is recursively estimated as stated in equation (13).

$$\mathrm{C_t} = \gamma \mathrm{C_{t-1}} + (1-\gamma)\left(y_t y_t^T\right) \tag{13}$$

The scalar $\gamma \in [0,1]$ controls how much memory the estimate retains: lower γ increases sensitivity to recent changes, while higher γ smooths fluctuations but slows adaptation. To isolate the measurement noise contribution from the total innovation spread, the measurement noise covariance is extracted by subtracting the state prediction uncertainty from the empirical innovation covariance using (14).

$$\mathrm{R_t} = \mathrm{C_t} - H\overline{P}_t H^T \tag{14}$$

This ensures that $\mathrm{R_t}$ captures only the measurement noise component, while the contribution of state prediction uncertainty ($H\overline{P}_t H^T$) is removed. When sensor conditions degrade (e.g., motion blur or checkerboard occlusion), $\mathrm{C_t}$ increases, which in turn increases $\mathrm{R_t}$, causing the filter to place less trust in the degraded measurements. This formulation enforces a physically meaningful separation between state uncertainty and sensor noise, consistent with the covariance matching principle. A parallel adaptation is performed in the state domain for the process noise covariance Q_t. Instead of using innovation residuals, the update uses the correction applied to the state estimate during the EKF update step mentioned in equation (15).

$$Q_t = \lambda Q_{t-1} + (1-\lambda)(\widehat{x}_t - \overline{x}_t)(\widehat{x}_t - \overline{x}_t)^T \tag{15}$$

The positive semi-definiteness of both $\mathrm{Q_t}$ and $\mathrm{C_t}$ is guaranteed by construction, as each is computed as a convex combination of a previous positive semi-definite matrix and an outer product term. For $\mathrm{R_t}$ (Eq. (14)), the subtraction of $H\overline{P}_t H^T$ from $\mathrm{C_t}$ may yield non-positive-semi-definite results during transient periods when predicted state uncertainty temporarily exceeds the empirical innovation spread. In implementation, eigenvalue clamping is applied to enforce a minimum noise floor, ensuring that $\mathrm{R_t}$ remains positive semi-definite at every time step. The forgetting factors were selected empirically based on the motion characteristics observed during the UAV indoor flight. Specifically, $\gamma = 0.95$ was used for the measurement noise adaptation, corresponding to an effective window of

approximately 20 samples, and $\lambda = 0.98$ was used for the process noise adaptation, corresponding to an effective window of approximately 50 samples. Sensitivity analysis showed that the system maintained sub-millimeter RMSE for $\gamma \in [0.90, 0.98]$ and $\lambda \in [0.95, 0.99]$, indicating reasonable robustness to the specific choice of forgetting factors.

2.5. Laser correction and displacement output

The laser provides a direct scalar measurement of the distance between the platform and the structure. However, since the platform is also rotating during measurement, the laser beam deviates from the nominal transverse axis and so includes both the structure's displacement and the platform's motion. To correct for this angular deviation, the raw measurement is projected onto the transverse axis using the pitch angle θ_y and yaw angle θ_z extracted from the EKF-estimated quaternion q_t. θ_y denotes the pitch angle (rotation

Table 1
Developed system components specification.

Components	Picture	Model	Specification
Camera		Samsung Galaxy S21	12 MP wide-angle, 12 MP ultra-wide (123° FoV), 64 MP telephoto (3x zoom); 4 K @ 60 fps video
IMU		GY-9: MPU-9250 + BMP280	Gyro: ±250–2000 degree/s, Accel: ±2–16 g, 16-bit resolution, 3–5 V operating voltage
Laser on the drone		Keyence IL-2000	Resolution: 100 μm, Range: ±9999.9 mm, Display rate: ~10 Hz, Output: ±5 V / 4–20 mA
Hexapod		Acrome Stewart Platform	Payload: 12 kg, Range: ±60 mm (XY), ±50 mm (Z), ±20 degree (angles), Repeatability: ±100 μm
LVDT – ground truth		DCV150A – RDP Group	±150 mm measurement range, Excitation: 14–26 V, Output: 0–10 V, Supply: 30 mA
Laser – ground truth		Polytec RSV-150	Range: up to 300 m, Resolution: 1 μm, Bandwidth: up to 2 MHz
Vicon camera		Valkyrie 16	Resolution: 26 MP, High-speed frame rates, sub-mm accuracy, IR tracking with 10-camera setup

about the body y-axis) and θ_z denotes the yaw angle (rotation about the body z-axis), both obtained by converting q_t to Euler angles. The rotation-corrected laser distance is computed using equation (16).

$$L_c = L\cos(\theta_y)\cos(\theta_z) \tag{16}$$

where L is the raw laser range measurement. This correction accounts for geometric foreshortening: when the platform rotates, the laser overestimates the transverse distance by a factor of $1/(\cos\theta_y \cos\theta_z)$. The corrected absolute transverse displacement of the structure is then computed by subtracting the UAV's translational movement using equation (17).

$$D_T(t) = -[(L_c(t) - L_c(t_0)) - (p_T(t) - p_T(t_0))] \tag{17}$$

where $p_T(t)$ is the EKF-estimated translation in the transverse direction at time t, and t_0 is the reference time when displacement measurement starts. This final step enables accurate, reference-free displacement estimation by compensating for both rotational and translational platform motion. Critically, the laser is excluded from the EKF and corrected post-filter, avoiding the need for a structural dynamics model within the filter.

2.6. Computational cost

The computational cost of the proposed method is dominated by two components: camera pose estimation via bundle adjustment and the EKF prediction-update cycle. The EKF operates on a 16-dimensional state vector (Eq. (2), resulting in $O(n^3) = O(4096)$ operations per cycle, which requires approximately 0.4 ms per step on a desktop computer (Intel Core i7, MATLAB R2023b). At the IMU update rate of 100 Hz, this leaves a per-cycle budget of 10 ms, which is comfortably met. The camera pose estimation is more computationally intensive, requiring approximately 20 ms per frame, but operates at the lower camera frame rate of 30 fps (33.3 ms budget). All processing in the current study was performed offline; real-time implementation would require porting the MATLAB code to an optimized C/C++ implementation on a companion computer such as the NVIDIA Jetson series.

3. System development

A controlled experimental setup was developed using multiple sensing devices and data acquisition (DAQ) systems to evaluate the accuracy of the proposed displacement estimation method. This system included several components described in Table 1. Each component in the setup was selected based on its ability to capture specific motion or displacement parameters of the UAV or the bridge. The IMU and a front-mounted laser were installed on the UAV to measure its dynamic movement and relative distance to the bridge, with data collected through an Arduino Nano microcontroller. A mobile camera was also attached to the UAV to track its motion visually. These three components were all intended to be mounted on a carbon bar, which was designed to eventually attach to a UAV. This setup aimed to minimize the distance between the laser and the target structure, addressing the limited sensing range of the laser as noted in [48]. For ground-truth measurements, a high-speed Vicon motion tracking system was used to record the UAV's position and orientation, while two ground-based sensors, an LVDT and a laser vibrometer, monitored the bridge's displacement with high temporal resolution using Dewesoft DAQ. The UAV was actuated using a programmable hexapod platform to simulate various translational and rotational motions. Post-processing included synchronization of all recorded signals using timestamps and cross-correlation methods to ensure accurate alignment for comparison. It is important to note that the Vicon motion capture system serves exclusively as a reference for characterizing hexapod/UAV platform motion and is not a component of the proposed displacement estimation system. The system itself including camera, laser, and IMU is designed to be fully self-contained and requires no external reference infrastructure during operation. Ground truth for structural (board) displacement is independently provided by the LVDT and laser vibrometer, both of which are field-deployable instruments commonly used in bridge monitoring practice.

Table 2 summarizes the specifications and roles of each experimental component used in the study.

4. UAV indoor flight

It is important to understand and replicate the motion characteristics of an actual UAV to ensure the proposed displacement estimation system functions effectively in real-world scenarios. UAVs, particularly during flight near bridge structures, experience various translational and rotational movements. These motions can introduce measurement errors if not properly accounted for in the system. Planned field operations require close-proximity flight in a confined space; therefore, the pilot was trained to maintain a safe stand-off to the structure while executing slow, low-amplitude translations and small rotations typical of this setting.

The UAV used for this comparison was the DJI Matrice 600 Pro, which was flown indoors under controlled conditions. A high-resolution Vicon motion capture system, consisting of ten infrared cameras, tracked the UAV's movement with sub-millimeter accuracy (0.2 mm) [55] across the entire capture volume with 100 Hz data acquisition capability. Four reflective markers were placed on the UAV to capture 6DOF. Fig. 2 shows the Vicon setup used to capture the UAV trajectory with the reflective markers attached to it for cameras to be able to detect the UAV object.

The data collected during the 25-second flight showed several important findings. Fig. 3 shows a sample dataset of indoor flight, highlighting translational motion and orientation changes. The pilot was trained to maintain 2–3 m standoff distances with translational movements at 0.1–0.5 m/s and angular velocities limited to ± 5 degree/s to simulate realistic inspection operations. The data collected during the flight showed several important characteristics. Translational motion was relatively stable, with oscillations

Table 2
Experimental settings and data acquisition configuration.

Component	Used in experiment	Sampling rate / Frame rate	DAQ device	Purpose in experiment
IMU	Mounted on carbon bar (UAV)	100 Hz	Arduino Nano (microcontroller)	Measure UAV translation and rotation
Drone Laser	Front-mounted on UAV	45 Hz	Arduino Nano (microcontroller)	Relative displacement between UAV and bridge
Mobile Camera	Mounted on carbon bar (UAV)	30 fps	Internal memory	Measure UAV translation and rotation
Vicon System	Tracks markers on UAV	100 fps	Vicon Tracker software	Ground-truth UAV position and orientation
LVDT Sensor	In contact with board (bridge)	1000 Hz	Dewesoft DAQ	Ground-truth displacement of the bridge
Laser Vibrometer	Fixed, pointed at board	1000 Hz	Dewesoft DAQ	High-resolution ground-truth for displacement of the bridge
Hexapod	Actuates carbon bar (UAV) attached to hexapod platform	Scripted motion (controlled)	Hexapod Acrome software	Generate translation/rotation for each test scenario

occurring at low frequencies (0.05–0.5 Hz). In contrast, rotational motion, particularly pitch, was more variable and introduced higher-frequency noise (0.3–1.5 Hz). Pitch motion showed the largest range (±7 degree) with strong correlation to longitudinal velocity changes, while roll motion exhibited rapid corrections (±3 degree) in response to translational commands, and yaw motion demonstrated smooth transitions (±2 degree) during commanded heading changes. This type of disturbance is especially relevant for displacement estimation, as it can affect the accuracy of laser-based measurements and the overall stability of the system.

Cross Power Spectral Density (CPSD) analysis, shown in Fig. 4, showed the frequency distribution of UAV motion energy. Translational motion exhibited primary energy concentration in the 0.5 Hz range corresponding to pilot-induced movements. Laboratory experiments were then designed to reflect this operational profile and its safety constraints. To evaluate and refine the system under repeatable conditions, a Stewart platform (hexapod) was used to simulate UAV motion in the laboratory.

5. Experiment setup and description

The research team set up an experiment in the laboratory to measure the out-of-plane displacement. Camera, IMU, and laser were attached to a carbon bar, which was connected to a hexapod platform capable of moving in 6DOF in order to mimic the UAV motion. The hexapod platform can receive any input in .csv format using Acrome software, as long as it falls within its range of motion mentioned in Table 1. In order to secure and fix the carbon bar to hexapod, a 3D-printed mounting part was used, preventing sliding or falling from the platform as shown in Fig. 5.

A phone camera was mounted on the carbon bar to record video of a 20 × 20 mm grid checkerboard pattern, which was used as a calibration reference. The camera was positioned downward to capture the checkerboard. Additionally, an IMU sensor and a laser were attached to the carbon bar. The IMU and camera moved together, capturing both rotational and translational motions. A wooden board was manually moved to simulate the lateral displacement of a railroad bridge pier, using field data collected from actual train crossings on bridges requiring repairs. To ensure the simulated movements accurately represent real-world railroad bridge behavior, the 1 in. transverse displacement used in all tests was selected based on field data collected by Moreu et al. [56] from a Class I timber railroad bridge under maintenance, with trains passing at approximately 24.1 km/h (15 mph). This bridge was considered representative of the broader bridge population of interest. While one person moved the board, an LVDT sensor and a Polytec RSV-150 laser, both connected to a Dewesoft system, measured its displacement. A set of 10 Vicon cameras was placed around the room to track the movement of the carbon bar throughout the test, providing reference measurements of hexapod movement. The entire test ran for approximately 30 s. The complete setup is shown in Fig. 6.

The controlled laboratory setting enables systematic isolation and evaluation of individual motion components which would be infeasible in field conditions due to environmental variability and limited repeatability. This stepwise approach provides a foundation for algorithm refinement before field deployment. To ensure realistic motion of hexapod based on the UAV flight data conducted earlier, the UAV flight data was processed and scaled to fit within hexapod operational limits while preserving critical motion characteristics. Translational motion was scaled by a factor of 0.025 to accommodate hexapod constraints, while rotational motion was preserved at full scale within ± 20° limits. The frequency content was maintained through appropriate time scaling, ensuring that the essential dynamics needed to validate displacement estimation methods were replicated. Fig. 7 shows the CPSD of hexapod for a random motion profile as it was conducted in the UAV indoor flight.

The hexapod naturally generated smoother and more deterministic trajectories due to its mechanical actuation; however, comparison between scaled and original motion parameters demonstrated good agreement in dominant frequency content of both UAV and hexapod. Although UAV trajectories included broadband noise and occasional sharp directional changes, the hexapod replicated the essential dynamics needed to validate displacement estimation methods. The hexapod simulation had certain limitations including attenuation of high-frequency content (>10 Hz) due to bandwidth constraints, inability to replicate aerodynamic effects such as prop wash and air resistance, and simplified representation of control system feedback loops compared to actual UAV implementation. While the hexapod cannot replicate all aspects of actual flight conditions, it successfully reproduces the critical low-frequency motion components (0.1–5 Hz) that most significantly impact displacement estimation accuracy. The platform's ability to generate repeatable,

Fig. 2. UAV Indoor flight (a) UAV flight under Vicon camera, and (b) Reflective markers attached to the UAV.

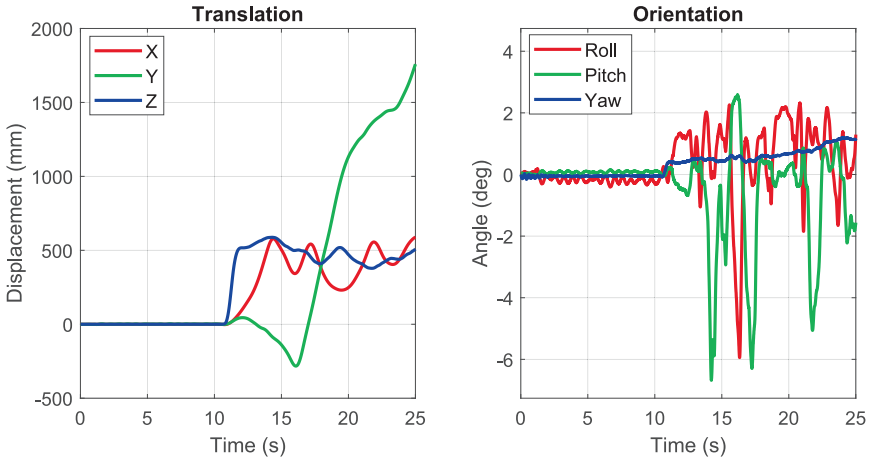

Fig. 3. UAV 6DOF motion recorded by Vicon cameras.

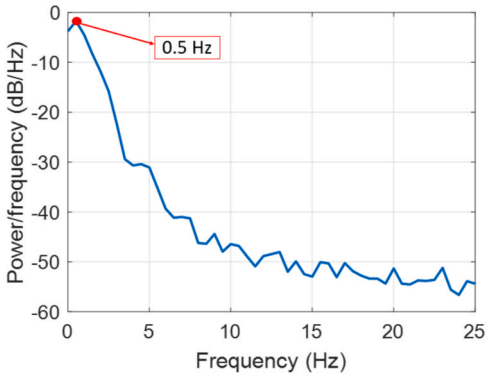

Fig. 4. CPSD of UAV.

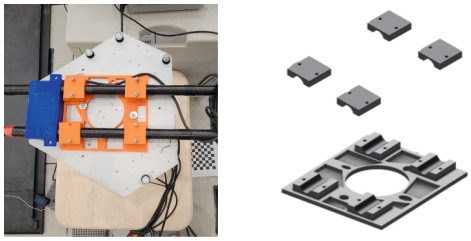

(a) (b)

Fig. 5. UAV motion simulator; (a) hexapod; and (b) mounting 3D printed part model.

programmable motion profiles enables systematic algorithm validation and performance characterization that would be impractical with actual UAV flights due to safety constraints, environmental variability, and reproducibility limitations. The controlled nature of hexapod testing allows for isolation of specific motion effects and provides a reliable foundation for sensor fusion algorithm development before field deployment, making it a suitable and practical alternative to indoor UAV flights for displacement estimation system validation.

Based on UAV flight analysis, the research team conducted four test scenarios in the laboratory to systematically evaluate different motion components. The research team conducted four different tests: (1) Translational Motion (Sinusoidal, 2 in. amplitude) involved pure translational motion, where the board moved in a sinusoidal pattern with a 2 in. amplitude; (2) Translational + Pitch Rotation (2 in. translation, 5 degree pitch rotation) included 2 in. amplitude translational board motion combined with 5 degree pitch rotations. This setup simulates scenarios where UAVs experience pitch oscillations, such as in turbulence or during flight stabilization; (3) Translational + Yaw Rotation (2 in. translation, 5 degree yaw rotation) which introduced 2 in. amplitude translational movement

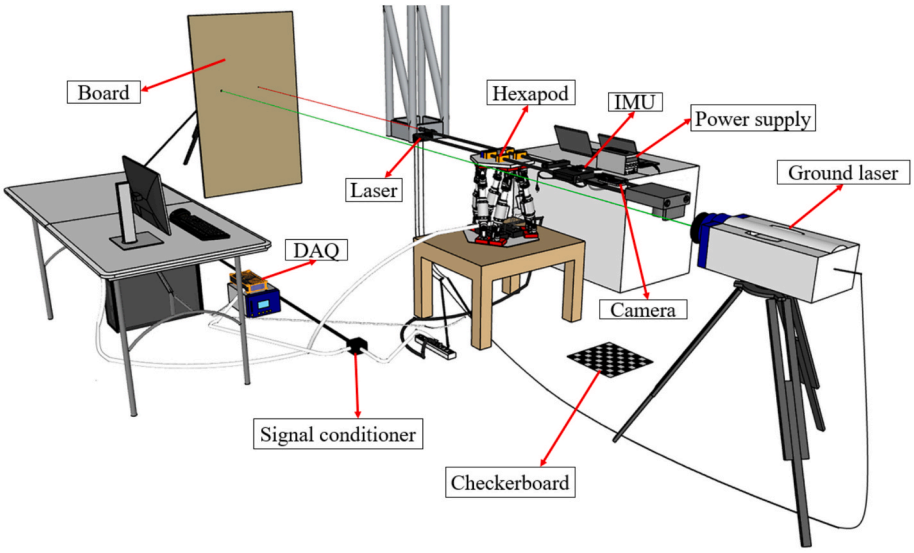

Fig. 6. 3D model of experiment setup and connections.

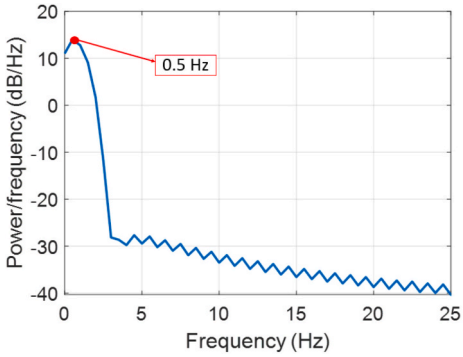

Fig. 7. CPSD of hexapod.

along with 5 degree yaw rotations. The setup mimics UAV movements during directional adjustments or turns, testing the system's ability to separate yaw-induced rotations from actual displacement measurements; and (4) Random Translational and Rotational Motion (1 in. random translation, 3 degree random rotation) which both translation and rotation followed a random pattern. Table 3 summarizes the test scenarios.

The roll movement of the UAV does not affect laser measurements so it has not been considered in any of the tests. These tests were designed to evaluate the impact of translation and rotation on the system's displacement estimation accuracy.

6. Result and discussion

Six different data sources were recorded during the test: laser sensors, video, IMU, LVDT, ground laser, and Vicon system measurements. Among these, the LVDT, ground laser, and Vicon data acted as reference points to verify the accuracy of the results. Fig. 8 illustrates how the experiment was set up.

The ground laser operates without making contact, whereas the LVDT relies on physical contact to measure displacement. Both

Table 3
Test scenarios.

Test	Name	Scenario	Hexapod motion	Board motion
1	T	Translation only	Sinusoidal motion, 2 in. amplitude	1 in. translation
2	TP	Translation + Pitch	2 in. translation, 5 degree pitch rotation	1 in. translation
3	TY	Translation + Yaw	2 in. translation, 5 degree yaw rotation	1 in. translation
4	TR	Random Translation + Rotation	1 in. random translation, 3 degree random rotation	1 in. translation

tools were positioned at the same height on the board to maintain consistent measurements. The choice between them depends on the situation. For example, in field applications like tracking side-to-side movement of a railway bridge, using an LVDT might not be practical due to installation challenges making the ground laser a more suitable alternative. In this test, the LVDT had a sensitivity of 0.0692 mm/V, and the ground laser had a sensitivity of 4 mm/V. Both were used to cross-check the displacement values and ensure reliability in the ground-truth data. If one device missed a reading, the other could act as a backup to ensure the data remained reliable.

6.1. Validation

To evaluate the performance of the proposed fusion method, Fig. 9 shows the estimated transverse displacement time history for test TY. The left panel compares the displacement estimated by the proposed camera-laser-IMU fusion method against the LVDT ground truth and the camera-laser-only method [24]. The transverse displacement $D_T(t)$ (Eq. (17)) represents the out-of-plane movement of the board (simulating a railroad bridge pier) along the laser beam axis, after compensating for platform rotation and translation. The right panel shows the physical setup with arrows indicating the positive (toward the sensor) and negative (away from the sensor) displacement directions. The board was manually pushed and pulled to simulate the lateral motion of a bridge pier under train loading, based on field data from Moreu et al. [56].

To evaluate the accuracy of the estimated displacement, results from the algorithm were compared against ground truth measurements using two error metrics: peak error (PE) and root mean square error (RMSE). These are defined in equations (18) and (19).

$$PE = \max(|\Delta e_i - \Delta m_i|) \tag{18}$$

$$RMSE = \sqrt{\frac{1}{N}\sum_{i=1}^{N}(\Delta e_i - \Delta m_i)^2} \tag{19}$$

Here, Δe_i represents the displacement estimated by the algorithm, Δm_i is the displacement recorded by the reference sensor, and N is the number of data points. These metrics offer a clear way to assess how closely the estimated values match the ground truth.

As trains pass over a bridge, the structure undergoes repetitive lateral deflection under successive axle loads. Peak-to-peak displacement quantifies the total range of movement within one loading cycle and is commonly used by engineers to evaluate whether structural response remains within safe operational limits. In this study, one cycle is defined by three consecutive extrema: Max1 (the local maximum before the downward deflection), Min (the peak lateral deflection), and Max2 (the local maximum after the structure returns toward its resting position). Two maxima are needed because the bridge does not necessarily return to exactly the same position after each deflection due to residual vibration or shifting baseline. The peak-to-peak displacement for each cycle is therefore computed as Max(Max1, Max2) − Min, taking the larger of the two boundary maxima to capture the worst-case range of motion. Fig. 10 illustrates this calculation for cycle 1 of a transverse railroad bridge displacement record with nine loading cycles, similar to the simulated board movement in this study.

In this study, peak-to-peak values were calculated for both the fused and non-fused displacement data and then compared to reference measurements. A summary of the PE, RMSE, and peak-to-peak errors across four test cases, both with and without sensor fusion, is provided in Table 4.

Fig. 11 presents the peak-to-peak error across nine cycles in the time history, showing the method's capability to capture the complete range of otion. The results show that applying sensor fusion leads to a significant improvement in performance. On average, peak error is reduced from 5.64 mm to 1.74 mm, which corresponds to a 69.1% improvement. Similarly, the average RMSE drops from 2.93 mm to 0.93 mm, resulting in a 68.3% reduction. The reduction in peak error indicates that sensor fusion helps reduce large deviations that may occur due to sensor noise or drift, particularly during dynamic movements. For example, in the TY test, where transverse motion is combined with yaw rotation, the peak error w/o (without) fusion is 6.53 mm, but it drops to 1.33 mm with fusion,

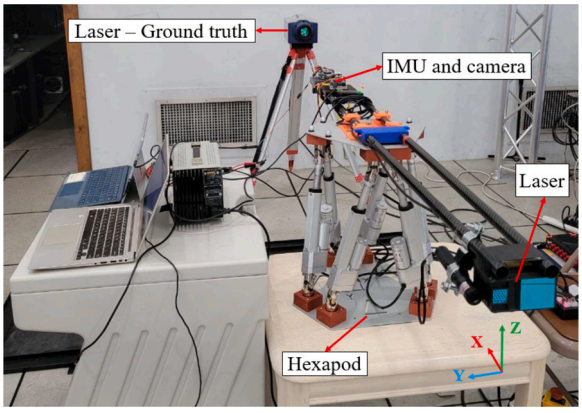

Fig. 8. Experiment setup.

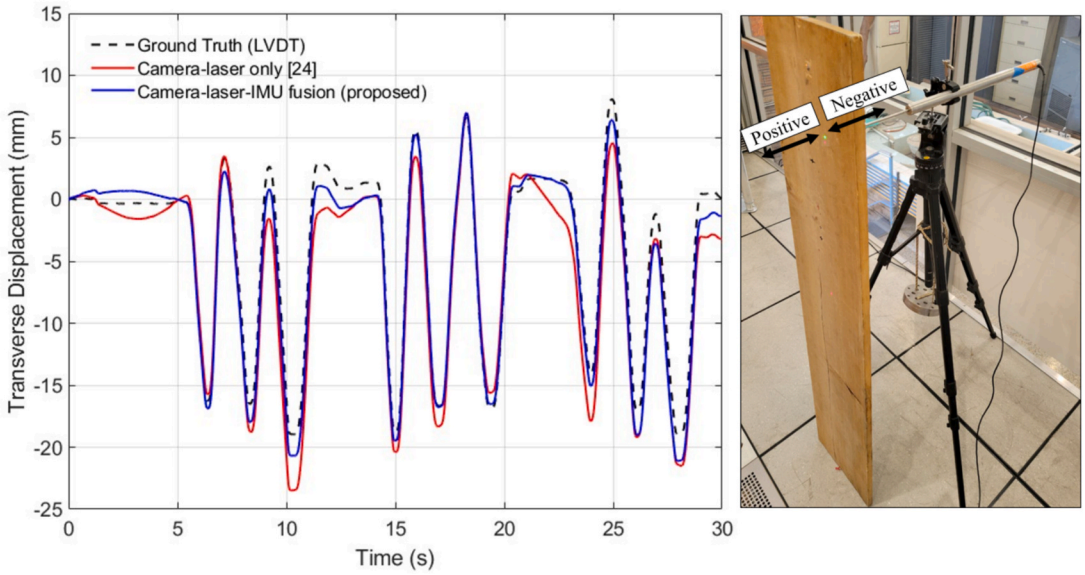

Fig. 9. Estimated transverse displacement time-history for the TY test.

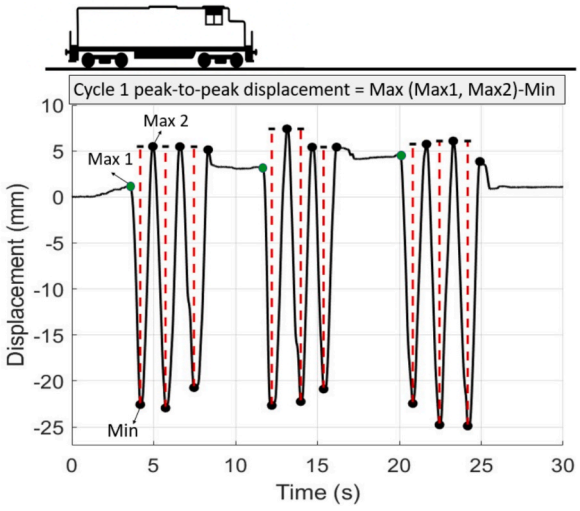

Fig. 10. An example of peak-to-peak displacement calculation for cycle 1.

Table 4
Displacement estimation errors with and without sensor fusion.

Test	PE (mm)		RMSE (mm)		Peak-to-peak (mm)	
	w/o fusion	w fusion	w/o fusion	w fusion	w/o fusion	w fusion
T	4.61	2.41	2.33	1.24	1.41	0.47
TP	5.97	1.45	2.73	0.83	0.65	0.23
TY	6.53	1.33	3.60	0.78	1.78	0.90
TR	5.45	1.78	3.04	0.87	0.69	0.25
Average	5.64	1.74	2.93	0.93	1.13	0.46

an improvement of nearly 80%. This suggests that the fusion algorithm is especially effective in handling complex motion scenarios where single sensors may become less reliable. The RMSE results further support this observation. Tests like TP and TY show high RMSE values w/o fusion (2.73 mm and 3.6 mm, respectively), which are significantly reduced to below 1 mm with fusion. This demonstrates that the fusion method not only corrects for individual spikes but also enhances the overall stability of the displacement

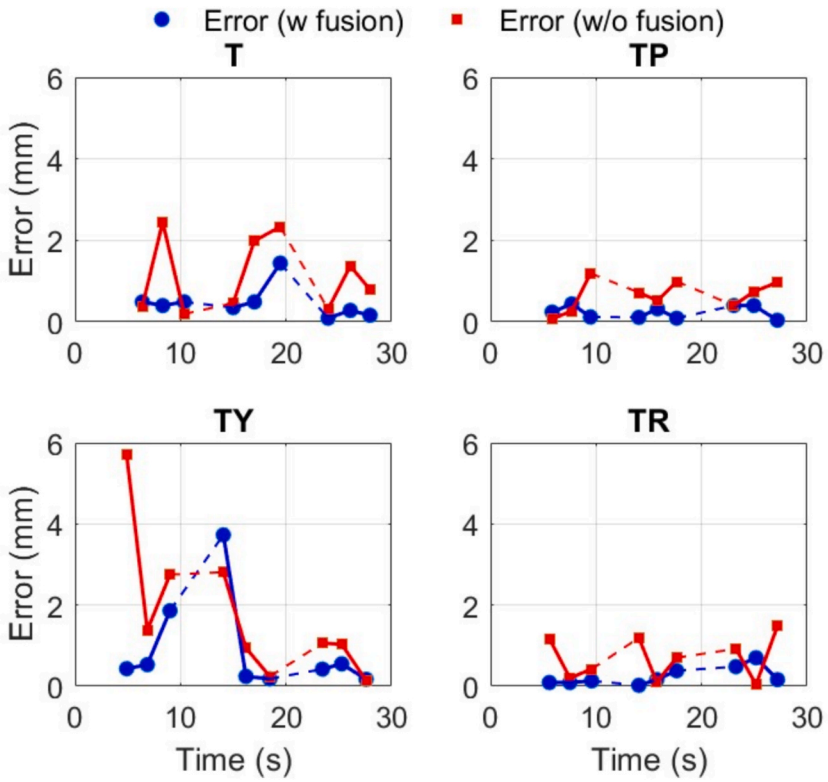

Fig. 11. Peak-to-peak errors in nine cycles across four tests.

estimate over time. The fusion approach appeared especially effective in dynamic or multi-axis motion cases like TY, where error margins were higher in the non-fused condition. This could be attributed to the fusion system's ability to compensate for noise or drift that may affect single-sensor estimates under complex movement. In TY test, the non-fused error spiked to nearly 6 mm at 4 s due to the combined effects of yaw and lateral motion. The fused method quickly reduced this peak to about 1.5 mm. Although both approaches leveled out by 16 s, the non-fused error increased again to 3.5 mm, while the fused method kept it below 1 mm. This quick correction showed that the fusion approach was more reliable in complex motion.

6.2. *Estimated displacement error sensitivity to hexapod platform motion*

Each test scenario was designed to isolate specific translational and rotational degrees of freedom to evaluate the influence of different motion components on measurement accuracy. Fig. 12 compares the distribution of peak-to-peak errors for both the non-fusion and sensor fusion approaches. The TY scenario which combined lateral translation with yaw rotation, resulted in the largest peak-to-peak displacement errors. This indicates that combined motion types, particularly those involving rotation, significantly reduce the performance of the camera-laser system.

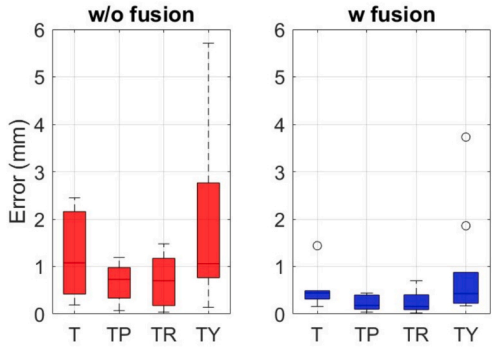

Fig. 12. Peak-to-peak error distribution comparison.

The non-fusion setup, relying only on the camera-laser configuration, showed increased error magnitudes under complex motion especially during the TY scenario, where median errors approached 2.5 mm. These deviations were attributed to the camera's limited ability to maintain accurate tracking under rotational disturbances. In contrast, sensor fusion consistently reduced both the magnitude and variability of errors across all motion types. Even under the challenging TY condition, the fused system maintained sub-millimeter error levels, demonstrating its capability to decouple and correct for the effects of combined translational and rotational movements. Fig. 13 shows the correlation of errors with 6DOF motion parameters for both methods.

Correlation analysis showed how specific motion types impacted measurement accuracy. For example, w/o fusion, X-translation showed a relatively high correlation with error (around 0.4), indicating that lateral motion introduced significant distortion likely due to changes in the angle of laser reflections. This finding showed the importance of sensor placement and orientation in UAV system design. Pitch motion showed consistently high correlation values (around 0.25) in both fused and non-fused cases. This suggested that pitch-related errors were not fully addressed by current fusion methods and might have required additional compensation strategies. Meanwhile, fusion led to a clear reduction in the correlation of errors with roll, yaw, and X-translation, showing that the algorithm effectively isolated and compensated for these motion effects. On the other hand, the small increase in correlation for Y and Z translations when using fusion suggested that new sources of error became more noticeable once the main ones were reduced. This showed that measurement errors came from multiple layers, and it was important to use motion compensation strategies that addressed all types of movement together, rather than looking at them one by one.

Fig. 14 presents the 6DOF time histories of the carbon bar measured by the Vicon motion-capture system across the four tests, together with the ground-based laser measurement of board displacement. The research team conducted an additional analysis focusing on the phase shift between translational motion in the X-direction and the corresponding ground-truth board movement obtained from laser-based measurements to further investigate the potential impact of temporal misalignment on localization accuracy. In this analysis, three discrete phase shift levels were defined as shown in Table 5 to simulate varying degrees of synchronization between the estimated and actual movement signals. These phase shift categories were determined by evaluating the alignment of peaks and valleys between the two signals.

Using this categorization, all 36 data points were analyzed to determine their respective phase relationships. For each point, the 6DOF transformation parameters including roll, pitch, yaw, and translations in X, Y, and Z directions were extracted. The average localization error under sensor fusion conditions was also computed for each phase category. These results are summarized in Table 6.

The analysis demonstrated that phase alignment between estimated translation in the X-direction and ground truth board movement had an impact on localization accuracy. When signals were in phase, the system achieved the lowest average error (0.22 mm), indicating optimal sensor fusion performance. As the phase shift increased, especially in the moderate range (45–90 degrees), the error rose significantly (0.80 mm), suggesting that even partial desynchronization could degrade fusion accuracy. Interestingly, in the out-of-phase condition (135–180 degrees), the system still maintained a moderate error level (0.40 mm), reflecting some robustness in the fusion algorithm.

The physical mechanism underlying phase-dependent errors relates to the displacement correction. When the UAV translational motion ($p_T(t)$) and the structural displacement occur in phase, the correction term ($p_T(t) - p_T(t_0)$) accurately tracks the UAV's contribution to the laser reading change, allowing clean isolation of the structural displacement. However, when a moderate phase shift exists (45–90°), the correction is partially misaligned: the UAV may be accelerating in one direction while the structure is near its displacement peak, causing the correction to overshoot or undershoot during the transition periods. This produces systematic residual errors that the EKF's adaptive mechanism can only partially mitigate. The somewhat counterintuitive result that out-of-phase conditions (135–180°) produce lower errors than moderate phase shifts (0.40 mm vs. 0.80 mm) can be explained by predictability: fully anti-correlated motion creates a more slowly varying, consistent correction error that the adaptive filter can better track over time.

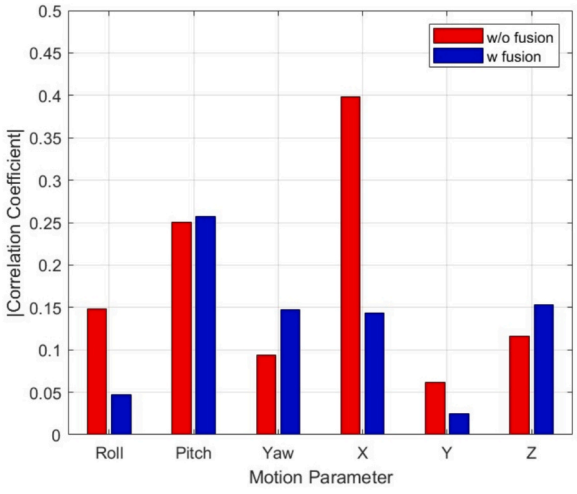

Fig. 13. Correlation between peak-to-peak error and 6DOF motion parameters for w/o fusion (NASIMI) and w fusion approach (this study).

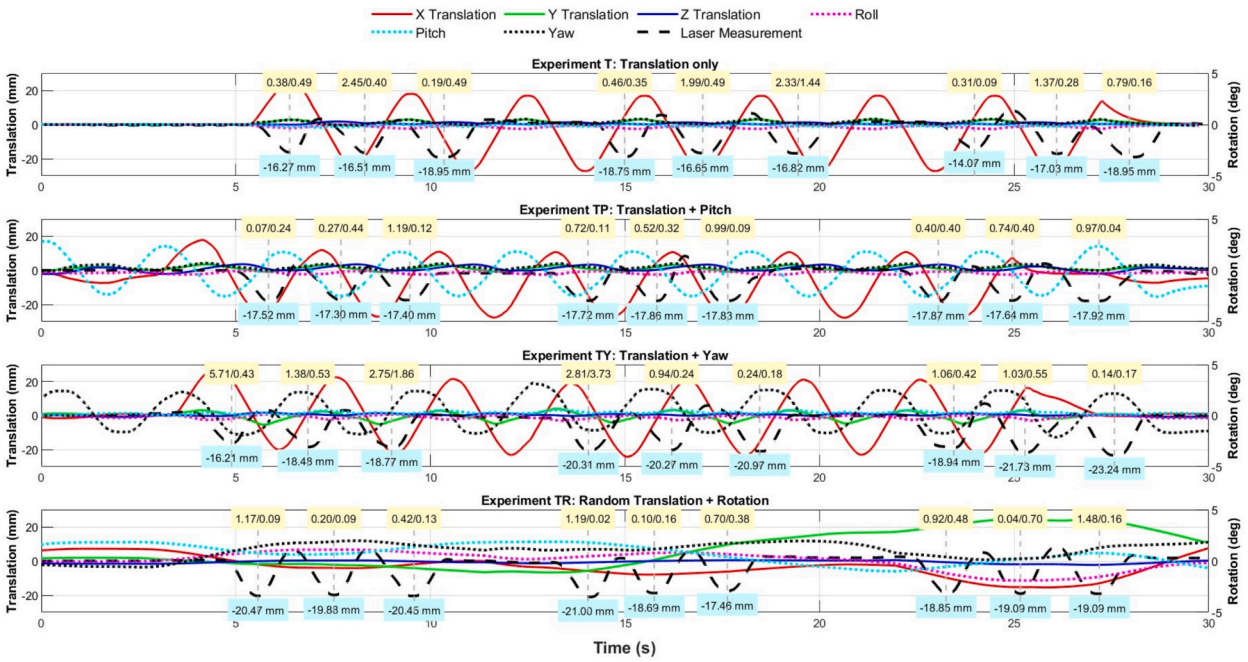

Fig. 14. Vicon 6DOF motion and laser displacement for tests T, TP, TY, and TR. Solid curves are translations (mm), dotted curves are rotations (deg), dashed black is the ground truth laser readings. Yellow boxes show non-fused/fused peak-to-peak errors per cycle; blue boxes show laser displacement readings (mm) at the location of peak-to-peak. (For interpretation of the references to colour in this figure legend, the reader is referred to the web version of this article.)

Table 5
Phase shift categories.

Phase Shift (degree)	Description
0 (In Phase)	Perfect alignment of peaks and valleys
45–90	Slight to significant lag
135–180 (Out of Phase)	Peaks of one align with valleys of the other

Table 6
Phase shift categories and average 6DOF.

Phase category	Roll (degree)	Pitch (degree)	Yaw (degree)	X (mm)	Y (mm)	Z (mm)	Avg error w fusion (mm)
In Phase	0.09	0.32	0.35	15.54	−0.21	1.29	0.22
Moderate Shift	0.21	0.16	0.15	4.86	−0.55	1.06	0.80
Out of Phase	0.23	−0.31	0.77	−4.91	−1.04	0.36	0.40

From a measurement synchronization perspective, the different sampling rates of the sensors (IMU at 100 Hz, laser at 45 Hz, camera at 30 fps) introduce inherent temporal misalignment. The EKF's asynchronous update capability partially mitigates this by performing prediction steps between measurement arrivals, but residual phase errors remain, particularly when sensor updates are not uniformly distributed within each sampling period.

This phase sensitivity has direct implications for structural dynamics. In operational modal analysis, accurate phase relationships are essential: as shown by Qin et al. [57] mode shapes require phase differences of either 0° or 180° between measurement points. The intermediate misalignment (45–90°) observed here would, if uncorrected, corrupt these modal phase relationships and could lead to incorrect mode identification or false damage detection. This aligns with findings that temporal misalignment introduces systematic errors that propagate into modal parameter identification.

The results reveal three primary conditions under which the system's performance degrades. First, yaw-translation coupling (TY scenario) produced the highest non-fused errors (PE = 6.53 mm, RMSE = 3.60 mm), identifying this as the most error-prone motion combination for camera-laser systems without IMU compensation. Although fusion reduced these errors substantially (PE = 1.33 mm, RMSE = 0.78 mm), the TY scenario still exhibited the largest fused peak-to-peak error (0.90 mm), indicating residual sensitivity. Second, pitch motion showed persistently high correlation with error (~0.25) regardless of fusion, suggesting that vertical tilting effects are not fully compensated by the current EKF formulation, which corrects laser measurements but does not explicitly model the

nonlinear coupling between pitch and out-of-plane displacement. Third, moderate phase misalignment (45–90°) between platform translation and structural movement produced higher errors (0.80 mm) than either in-phase (0.22 mm) or out-of-phase (0.40 mm) conditions, indicating that intermediate desynchronization where the correction is partially but inconsistently applied, is more detrimental than fully opposed motion, as the filter receives conflicting information that violates its linearized error dynamics assumptions. These findings suggest that future system refinements should prioritize enhanced pitch compensation, possibly through a dedicated pitch correction term in Equation (16), and improved temporal synchronization between sensors to minimize phase-related errors. Testing under more extreme multi-axis coupling conditions (e.g., simultaneous large-amplitude pitch, yaw, and translation at higher frequencies) is planned for future validation using actual UAV platforms.

These results highlighted the complicated relationship between translational and rotational motion during UAV operation and their combined effect on displacement estimation accuracy. Among the motion components, yaw had the most visible impact on error, especially when it was not synchronized with translational movement. This observation emphasized the importance of addressing phase shift between motion signals. Correlation and phase shift analyses showed that while the fusion algorithm effectively reduced errors related to yaw and lateral translation, the system still showed some sensitivity to pitch motion. This may be due to vertical tilting effects that were not fully corrected by the current filtering approach.

6.3. *Comparative benchmarking with alternative non-contact methods*

To contextualize the performance of the proposed camera-laser-IMU fusion method within the broader landscape of non-contact displacement measurement, Table 7 summarizes the characteristics of major alternative approaches based on published literature. Direct experimental comparison with all methods is beyond the scope of this study; however, this literature-based synthesis contextualizes the relative strengths and limitations of each approach.

The comparison in Table 7 reveals that each method involves inherent trade-offs among accuracy, measurement direction, platform mobility, and cost. Vision-only methods offer excellent in-plane accuracy but cannot resolve out-of-plane displacement without additional depth information—a fundamental limitation for transverse bridge monitoring from moving platforms. Radar and LDV provide high precision but require stationary deployment or stable references, making them poorly suited for UAV-based measurement where platform motion is unavoidable. The camera-laser system of Nasimi and Moreu [24] first enabled out-of-plane measurement from UAVs but remained sensitive to rotational motion, which the present work addresses through IMU fusion.

The average RMSE of 0.93 mm achieved by the proposed fusion method compares favorably to reported vision-only field accuracy (1–2 mm), while explicitly addressing the out-of-plane measurement gap. Even under the most challenging scenario (TY), the fused RMSE remained below 0.8 mm. This accuracy is sufficient for many structural monitoring applications, where displacement thresholds for damage identification in railroad bridges are typically 3–5 mm. However, laboratory validation represents best-case performance; field deployment will introduce additional challenges including variable lighting, wind-induced platform disturbances, and natural feature tracking.

7. Limitation and future work

This study was conducted under controlled laboratory conditions that, while enabling systematic and repeatable validation, introduce limitations for field deployment. Specific environmental factors not captured include: (a) wind and aerodynamic disturbances causing higher-frequency, less predictable platform motion than the hexapod simulates, potentially degrading camera tracking through increased motion blur and IMU accuracy through vibration; (b) lighting variability affecting camera-based checkerboard detection, motivating future transition to markerless tracking using natural surface features; (c) surface material variability on real bridges (concrete, steel, timber) affecting laser reflectance characteristics; and (d) electromagnetic interference near railroad infrastructure. The deliberate choice of laboratory validation was motivated by the need to isolate specific motion effects and quantify their

Table 7
Comparison of non-contact displacement measurement approaches.

Method	Measurement Direction	Platform Tolerance	Typical Accuracy	UAV-Compatible	Key Limitation	Representative Studies
Vision-only (DIC/ template matching)	In-plane	Low	~0.04 mm (lab) to 1–2 mm (field)	Limited	Cannot directly measure out-of-plane displacement; sensitive to lighting	[12,13,14,15,16,17]
Ground-based radar interferometry	Line-of-sight	N/A (fixed)	0.01–0.1 mm	No	High cost; stationary; limited to line-of-sight	[42,43]
Laser Doppler vibrometry	Line-of-sight	Low–Moderate	<0.01 mm	Emerging [22]	Requires stable reference; expensive; single-point	[22,23]
Camera–laser	Out-of-plane	Low	1–5 mm with UAV motion	Yes	Sensitive to UAV rotation; no IMU compensation	[24,47,48]
LiDAR	3D point cloud	Moderate	1–10 mm	Emerging	Lower accuracy for dynamic displacement; limited by scanning rate	[38,59]
Camera–laser–IMU (this study)	Out-of-plane	Moderate–High	<2 mm (lab)	Designed for UAV	Validated only in lab; requires target	—

individual contributions. The controlled experiments established that the fusion algorithm achieves sub-millimeter RMSE under repeatable motion profiles, providing a performance baseline against which future field results can be compared.

Additionally, the hexapod platform, while accurately reproducing programmed motions, cannot fully replicate the dynamic characteristics of actual UAV flight, including complex 6DOF maneuvers, interactions between onboard control algorithms, and exposure to wind gusts and high-frequency vibrations. A formal stability proof of the adaptive EKF under general nonlinear UAV motion conditions remains an open problem in the filtering literature. While the positive semi-definiteness of the adapted covariances is guaranteed by construction, convergence guarantees for innovation-based adaptive Kalman filters under nonlinear dynamics are an active area of research. Future work should investigate the theoretical convergence bounds of the proposed adaptive mechanism under realistic UAV flight conditions. Moreover, the current system performs all data processing offline, which introduces latency and restricts applicability for time-sensitive or real-time monitoring scenarios. A fully integrated onboard system with real-time data acquisition and processing capabilities will be necessary for operational use.

The accurate displacement estimates from our sensor fusion framework can serve as input to inverse methods for structural response reconstruction, including modal identification, force reconstruction, and damage detection. While the inverse techniques in [58] address different structural typologies, combining high-fidelity displacement measurements with inverse structural identification represents a promising direction for comprehensive structural assessment.

The 1 in. simulated bridge displacement, while representative of values reported in literature [56], was applied uniformly across test scenarios. In practice, displacement amplitudes vary significantly depending on bridge type, train loading, and span characteristics, and may include broader frequency content and noisier conditions. Future validation should therefore include a wider range of displacement magnitudes and environmental noise levels to evaluate system performance under diverse and realistic conditions. Furthermore, tests were conducted at relatively short distances, and the impact of increasing UAV-to-target range which is necessary for safe operation around active railroad infrastructure on measurement accuracy and sensor performance remains unquantified. This study successfully demonstrates significant improvements in displacement estimation accuracy (69.1% reduction in peak error, 68.3% reduction in RMSE) through sensor fusion in controlled conditions, however, the findings should be interpreted within these limitations. To bridge the gap between laboratory validation and field deployment, the following roadmap is planned: (1) outdoor stationary tests evaluating the system under varying lighting and weather with a fixed tripod; (2) outdoor UAV hover tests at fixed standoff distance to characterize real flight noise; (3) controlled bridge tests on an instrumented bridge with known displacement; and (4) progressive extension to diverse bridge types and loading conditions.

8. Conclusion

This study developed and experimentally validated a camera-laser-IMU system for non-contact transverse displacement estimation of railroad bridges, targeting applications where conventional sensor installation is impractical or unsafe. The proposed method enhanced displacement estimation accuracy over prior approaches by incorporating an IMU into an existing camera-laser framework and applying an EKF with innovation-based adaptive noise tuning. Controlled laboratory testing using a 6DOF hexapod platform simulated realistic UAV motion across four scenarios including pure translation (T), translation with pitch (TP), translation with yaw (TY), and combined random motion (TR). The sensor fusion approach achieved substantial improvements, reducing peak error by 69.1% and RMSE by 68.3%, with the lowest error observed under yaw-induced motion. Error correlation and phase-shift analyses showed that motion coupling, particularly between yaw rotation and lateral translation, increases displacement estimation errors when not properly addressed. Conversely, phase-aligned motion between estimated translation and ground-truth movement yielded the most accurate results. While the fusion method effectively decreased the majority of translational and rotational disturbances, residual sensitivity to pitch motion remained, indicating the need for further refinement in compensating for vertical-axis tilting effects. These results highlight the importance of dynamic motion modeling, temporal alignment, and multi-sensor integration in UAV-based structural health monitoring systems. Promising laboratory performance was achieved; however, several limitations remain. The hexapod platform, while capable of replicating 6DOF UAV dynamics, does not fully capture real-world UAV control feedback, environmental disturbances, or flight-induced instabilities. Additionally, the use of simplified targets and constrained sensing ranges necessitates future validation under operational field conditions. The proposed system presents a scalable, reference-free displacement monitoring approach aligned with broader SHM goals for aging transportation infrastructure. Future efforts will focus on validating system performance in diverse environmental and operational contexts to support safe and cost-effective UAV-based bridge inspections.

CRediT authorship contribution statement

Mahsa Sanei: Writing – original draft, Visualization, Validation, Methodology, Investigation, Formal analysis, Conceptualization. **Piedad Miranda-Chiquito:** Writing – original draft, Validation, Methodology, Data curation, Investigation, review & editing. **G. Matthew Fricke:** Writing – review & editing, Validation, Software, Resources, Data curation. **Fernando Moreu:** Writing – review & editing, Supervision, Resources, Project administration, Funding acquisition, Conceptualization.

Declaration of competing interest

The authors declare that they have no known competing financial interests or personal relationships that could have appeared to influence the work reported in this paper.

Acknowledgement

The authors appreciate the support of the Federal Railway Administration (FRA) BAA project number 693JJ621C000010; the National Science Foundation, Division of Information & Intelligent Systems (IIS), CISE, Hardening the Data Revolution DSC (Grant/Award No. 2123346); the U.S. Department of Transportation (Award No. 69A3552348306) through the USDOT Southern Plains Transportation Center (SPTC); the Office of Naval Research, Structural Reliability ONR 331 (Grant No. 13620990, Award No. N00014-22-1-2638), and the Office of Naval Research, Structural Reliability ONR 331 (Grant No. 13106652, Award No. N00014-21-1-2929). The author would like to thank the UNM Center for Advanced Research Computing, supported in part by the National Science Foundation, for providing the simulation space and the large-scale laboratory and testing area used indoors in this work. The authors would also like to appreciate the help and assistance from Michael Carl, and Ronan Reza.

Data availability

Data will be made available on request.

References

[1] "ASCE's, American Infrastructure Report Card," ASCE's 2021 Infrastructure Report Card | https://infrastructurereportcard.org/ 2021 Accessed: Oct. 11, 2024. [Online]. Available.
[2] G. Venturi, P. Simonsson, and P. Collin, "Strengthening old steel railway bridges: a review," in *In IABSE Congress 2021: Structural Engineering for Future Societal Needs*, Ghent, Belgium, Sep. 2021, pp. 1718–1727. doi: 10.2749/ghent.2021.1718.
[3] I.N. Robertson, Prediction of vertical deflections for a long-span prestressed concrete bridge structure, Engineering Structures 27 (12) (Oct. 2005) 1820–1827, https://doi.org/10.1016/j.engstruct.2005.05.013.
[4] F. Moreu, et al., Dynamic Assessment of Timber Railroad Bridges using Displacements, Journal of Bridge Engineering 20 (10) (Oct. 2015) 04014114, https://doi.org/10.1061/(ASCE)BE.1943-5592.0000726.
[5] H. Sekiya, K. Kimura, and C. Miki, "Technique for Determining Bridge Displacement Response Using MEMS Accelerometers," *Sensors*, vol. 16, no. 2, Art. no. 2, Feb. 2016, doi: 10.3390/s16020257.
[6] D. Hester, J. Brownjohn, M. Bocian, Y. Xu, Low cost bridge load test: calculating bridge displacement from acceleration for load assessment calculations, Engineering Structures 143 (Jul. 2017) 358–374, https://doi.org/10.1016/j.engstruct.2017.04.021.
[7] A. Hoag, N.A. Hoult, W.A. Take, F. Moreu, H. Le, V. Tolikonda, Measuring displacements of a railroad bridge using DIC and accelerometers, Smart Structures and Systems 19 (2) (2017) 225–236, https://doi.org/10.12989/sss.2017.19.2.225.
[8] M.O.A. Aqel, M.H. Marhaban, M.I. Saripan, N. Bt, Ismail, "Review of visual odometry: types, approaches, challenges, and applications,, SpringerPlus 5 (1) (Oct. 2016) 1897, https://doi.org/10.1186/s40064-016-3573-7.
[9] J.P. Lynch, Y. Wang, K.J. Loh, J.-H. Yi, C.-B. Yun, Performance monitoring of the Geumdang Bridge using a dense network of high-resolution wireless sensors, Smart Mater. Struct. 15 (6) (Oct. 2006) 1561, https://doi.org/10.1088/0964-1726/15/6/008.
[10] S. Jang, et al., Structural Health monitoring of a Cable-Stayed Bridge using Smart Sensor Technology: Deployment and Evaluation, Smart Structures and Systems 6 (Jul. 2010), https://doi.org/10.12989/sss.2010.6.5_6.439.
[11] F. Moreu, R.E. Kim, B.F. Spencer Jr., Railroad bridge monitoring using wireless smart sensors, Structural Control and Health Monitoring 24 (2) (2017) e1863.
[12] J.J. Lee, M. Shinozuka, A vision-based system for remote sensing of bridge displacement, NDT & E International 39 (5) (Jul. 2006) 425–431, https://doi.org/10.1016/j.ndteint.2005.12.003.
[13] T.H.T. Chan, et al., Vertical Displacement Measurements for Bridges using Optical Fiber Sensors and CCD Cameras — a Preliminary Study, Structural Health Monitoring 8 (3) (May 2009) 243–249, https://doi.org/10.1177/1475921708102108.
[14] D. Ribeiro, R. Calçada, J. Ferreira, T. Martins, Non-contact measurement of the dynamic displacement of railway bridges using an advanced video-based system, Engineering Structures 75 (Sep. 2014) 164–180, https://doi.org/10.1016/j.engstruct.2014.04.051.
[15] Z. Aliansyah, K. Shimasaki, T. Senoo, I. Ishii, and S. Umemoto, "Single-Camera-Based Bridge Structural Displacement Measurement with Traffic Counting," *Sensors*, vol. 21, no. 13, Art. no. 13, Jan. 2021, doi: 10.3390/s21134517.
[16] M.A. Garratt, J.S. Chahl, Vision-based terrain following for an unmanned rotorcraft, Journal of Field Robotics 25 (4–5) (2008) 284–301, https://doi.org/10.1002/rob.20239.
[17] H. Habeenzu, P. McGetrick, S. Taylor, D. Hester, UAS-based bridge displacement measurement using two cameras with non-overlapping fields of view, Automation in Construction 167 (Nov. 2024) 105687, https://doi.org/10.1016/j.autcon.2024.105687.
[18] D. Reagan, A. Sabato, and C. Niezrecki, "Unmanned aerial vehicle acquisition of three-dimensional digital image correlation measurements for structural health monitoring of bridges," in *Nondestructive Characterization and Monitoring of Advanced Materials, Aerospace, and Civil Infrastructure 2017*, SPIE, Apr. 2017, pp. 68–77. doi: 10.1117/12.2259985.
[19] D. T. Gillins, C. Parrish, M. N. Gillins, and Oregon State University, "Cost-Effective Bridge Safety Inspections Using Unmanned Aerial Vehicles (UAVS)," Oct. 2016. Accessed: Dec. 22, 2024. [Online]. Available: https://rosap.ntl.bts.gov/view/dot/37135.
[20] S. Abu Dabous and S. Feroz, "Condition monitoring of bridges with non-contact testing technologies," *Automation in Construction*, vol. 116, p. 103224, Aug. 2020, doi: 10.1016/j.autcon.2020.103224.
[21] C. Dong, S. Bas, N. Catbas, A completely non-contact recognition system for bridge unit influence line using portable cameras and computer vision, Smart Structures and Systems 24 (Nov. 2019) 617–630, https://doi.org/10.12989/sss.2019.24.5.617.
[22] P. Garg *et al.*, "Measuring Transverse Displacements Using Unmanned Aerial Systems Laser Doppler Vibrometer (UAS-LDV): Development and Field Validation," *Sensors*, vol. 20, no. 21, Art. no. 21, Jan. 2020, doi: 10.3390/s20216051.
[23] P. Garg, F. Moreu, A. Ozdagli, M.R. Taha, D. Mascareñas, Noncontact Dynamic Displacement Measurement of Structures using a moving Laser Doppler Vibrometer, Journal of Bridge Engineering 24 (9) (Sep. 2019) 04019089, https://doi.org/10.1061/(ASCE)BE.1943-5592.0001472.
[24] R. Nasimi, F. Moreu, Development and Implementation of a Laser–Camera–UAV System to measure Total Dynamic Transverse Displacement, Journal of Engineering Mechanics 147 (8) (Aug. 2021) 04021045, https://doi.org/10.1061/(ASCE)EM.1943-7889.0001939.
[25] D.K. Shaeffer, MEMS inertial sensors: a tutorial overview, IEEE Communications Magazine 51 (4) (Apr. 2013) 100–109, https://doi.org/10.1109/MCOM.2013.6495768.
[26] M. Kok, J.D. Hol, T.B. Schön, Using Inertial Sensors for Position and Orientation Estimation, FNT in Signal Processing 11 (1–2) (2017) 1–153, https://doi.org/10.1561/2000000094.
[27] S. Weiss, et al., Monocular Vision for long-term Micro Aerial Vehicle State Estimation: a Compendium, Journal of Field Robotics 30 (5) (2013) 803–831, https://doi.org/10.1002/rob.21466.
[28] A. Makadia and K. Daniilidis, "Correspondenceless Ego-Motion Estimation Using an IMU," in *Proceedings of the 2005 IEEE International Conference on Robotics and Automation*, Apr. 2005, pp. 3534–3539. doi: 10.1109/ROBOT.2005.1570657.

[29] F.M. Mirzaei, S.I. Roumeliotis, A Kalman Filter-based Algorithm for IMU-Camera Calibration: Observability Analysis and Performance Evaluation, IEEE Transactions on Robotics 24 (5) (Oct. 2008) 1143–1156, https://doi.org/10.1109/TRO.2008.2004486.
[30] L. Meronen, W. J. Wilkinson, and A. Solin, "Movement Tracking by Optical Flow Assisted Inertial Navigation," in *2020 IEEE 23rd International Conference on Information Fusion (FUSION)*, Jul. 2020, pp. 1–8. doi: 10.23919/FUSION45008.2020.9190586.
[31] C. Li, L. Yu, S. Fei, Real-Time 3D Motion Tracking and Reconstruction System using Camera and IMU Sensors, IEEE Sensors Journal 19 (15) (Aug. 2019) 6460–6466, https://doi.org/10.1109/JSEN.2019.2907716.
[32] W. Fang, L. Zheng, H. Deng, A motion tracking method by combining the IMU and camera in mobile devices, in: In *2016 10th International Conference on Sensing Technology (ICST)*, Nov, 2016, pp. 1–6, https://doi.org/10.1109/ICSensT.2016.7796235.
[33] J.D. Hol, T.B. Schön, H. Luinge, P.J. Slycke, F. Gustafsson, Robust real-time tracking by fusing measurements from inertial and vision sensors, J Real-Time Image Proc 2 (2) (Nov. 2007) 149–160, https://doi.org/10.1007/s11554-007-0040-2.
[34] C. V. Angelino, V. R. Baraniello, and L. Cicala, "UAV position and attitude estimation using IMU, GNSS and camera," in *2012 15th International Conference on Information Fusion*, Jul. 2012, pp. 735–742. Accessed: Oct. 13, 2024. [Online]. Available: https://ieeexplore.ieee.org/document/6289875/figures#figures.
[35] Y. Zhang, J. Tan, Z. Zeng, W. Liang, Y. Xia, Monocular camera and IMU integration for indoor position estimation, in: In *2014 36th Annual International Conference of the IEEE Engineering in Medicine and Biology Society*, 2014, pp. 1198–1201, https://doi.org/10.1109/EMBC.2014.6943811.
[36] M. B. Alatise and G. P. Hancke, "Pose Estimation of a Mobile Robot Based on Fusion of IMU Data and Vision Data Using an Extended Kalman Filter," *Sensors*, vol. 17, no. 10, Art. no. 10, Oct. 2017, doi: 10.3390/s17102164.
[37] A. Poulose and D. S. Han, "Hybrid Indoor Localization Using IMU Sensors and Smartphone Camera," *Sensors*, vol. 19, no. 23, Art. no. 23, Jan. 2019, doi: 10.3390/s19235084.
[38] Y. Zhao, Y. Liang, Z. Ma, L. Guo, H. Zhang, Localization and Mapping Algorithm based on Lidar-IMU-Camera Fusion, Journal of Intelligent and Connected Vehicles 7 (2) (Jun. 2024) 97–107, https://doi.org/10.26599/JICV.2023.9210027.
[39] C. Wang, T. Wang, J. Liang, Y. Chen, and Y. Wu, "Monocular vision and IMU based navigation for a small unmanned helicopter," in *2012 7th IEEE Conference on Industrial Electronics and Applications (ICIEA)*, Jul. 2012, pp. 1694–1699. doi: 10.1109/ICIEA.2012.6360998.
[40] J. Bednář, M. Petrlík, K. C. T. Vivaldini, and M. Saska, "Deployment of Reliable Visual Inertial Odometry Approaches for Unmanned Aerial Vehicles in Real-world Environment," in *2022 International Conference on Unmanned Aircraft Systems (ICUAS)*, Jun. 2022, pp. 167–176. doi: 10.1109/ICUAS54217.2022.9836067.
[41] Z. Ma, J. Choi, H. Sohn, Three-dimensional structural displacement estimation by fusing monocular camera and accelerometer using adaptive multi-rate Kalman filter, Engineering Structures 292 (Oct. 2023) 116535, https://doi.org/10.1016/j.engstruct.2023.116535.
[42] M. Pieraccini, M. Fratini, F. Parrini, C. Atzeni, Dynamic monitoring of Bridges using a High-speed Coherent Radar, IEEE Transactions on Geoscience and Remote Sensing 44 (11) (Nov. 2006) 3284–3288, https://doi.org/10.1109/TGRS.2006.879112.
[43] C. Gentile, G. Bernardini, An interferometric radar for non-contact measurement of deflections on civil engineering structures: laboratory and full-scale tests, Structure and Infrastructure Engineering 6 (5) (Oct. 2010) 521–534, https://doi.org/10.1080/15732470903068557.
[44] J. Yuan, Y. Zhou, Y. Zhang, and M. Abdel Wahab, "A large-stroke and adjustable-load magnetic quasi-zero stiffness isolator," *Mechanical Systems and Signal Processing*, vol. 239, p. 113326, Oct. 2025, doi: 10.1016/j.ymssp.2025.113326.
[45] Y. Zhou, F. Yao, Y. Wang, C. Bai, S. Liu, and M. Abdel Wahab, "Free vibration of orthotropic rectangular mindlin plates via spectral element model under arbitrary boundary conditions," *Thin-Walled Structures*, vol. 216, p. 113679, Nov. 2025, doi: 10.1016/j.tws.2025.113679.
[46] Y. Zhou, F. Yao, C. Bai, K. Li, S. Zhu, and M. Abdel Wahab, "Bandgap characteristics of periodic mindlin plates under arbitrary boundary conditions via the Spectral Element Method," *Thin-Walled Structures*, vol. 205, p. 112370, Dec. 2024, doi: 10.1016/j.tws.2024.112370.
[47] R. Nasimi, F. Moreu, M. Nasimi, R. Wood, Developing Enhanced Unmanned Aerial Vehicle Sensing System for Practical Bridge Inspections using Field Experiments, Transportation Research Record 2676 (6) (Jun. 2022) 514–522, https://doi.org/10.1177/03611981221075618.
[48] R. Nasimi, F. Moreu, A methodology for measuring the total displacements of structures using a laser–camera system, Computer-Aided Civil and Infrastructure Engineering 36 (4) (2021) 421–437, https://doi.org/10.1111/mice.12652.
[49] P. Sturm, "Pinhole Camera Model," in *Computer Vision: A Reference Guide*, K. Ikeuchi, Ed., Boston, MA: Springer US, 2014, pp. 610–613. doi: 10.1007/978-0-387-31439-6_472.
[50] Y. Furukawa and J. Ponce, "Accurate camera calibration from multi-view stereo and bundle adjustment," in *2008 IEEE Conference on Computer Vision and Pattern Recognition*, Jun. 2008, pp. 1–8. doi: 10.1109/CVPR.2008.4587681.
[51] "Stewart Platform: 6-DoF Hexapod Positioner System | Acrome." Accessed: Jul. 15, 2025. [Online]. Available: https://acrome.net/product/stewart-platform.
[52] R. Moghe, R. Zanetti, M.R. Akella, Adaptive Kalman Filter for Detectable Linear Time-Invariant Systems, Journal of Guidance, Control, and Dynamics 42 (10) (Oct. 2019) 2197–2205, https://doi.org/10.2514/1.G004359.
[53] D. C. Silva, A. Frutuoso, L. F. Souza, and E. A. de Barros, "Comparative Analysis of Innovation-Based Adaptive Kalman Filters Applied to AUVs Navigation," in *2022 Latin American Robotics Symposium (LARS), 2022 Brazilian Symposium on Robotics (SBR), and 2022 Workshop on Robotics in Education (WRE)*, Oct. 2022, pp. 31–36. doi: 10.1109/LARS/SBR/WRE56824.2022.9995869.
[54] A. Goel and D. S. Bernstein, "A Targeted Forgetting Factor for Recursive Least Squares," in *2018 IEEE Conference on Decision and Control (CDC)*, Dec. 2018, pp. 3899–3903. doi: 10.1109/CDC.2018.8619181.
[55] "Vicon Valkyrie | Advanced Motion Capture Cameras," Vicon. Accessed: Jul. 07, 2025. [Online]. Available: https://www.vicon.com/hardware/cameras/valkyrie/.
[56] F. Moreu, B.F. Spencer Jr., D.A. Foutch, S. Scola, Consequence-based management of railroad bridge networks, Structure and Infrastructure Engineering 13 (2) (Feb. 2017) 273–286, https://doi.org/10.1080/15732479.2016.1162817.
[57] S. Qin, J. Tang, J. Feng, Y. Zhou, F. Yang, M.A. Wahab, Modal parameter identification in civil structures via Hilbert transform ensemble with improved empirical wavelet transform, Journal of Vibration and Control 30 (7–8) (Apr. 2024) 1621–1634, https://doi.org/10.1177/10775463231166428.
[58] K.Q. Tran, T.V. Duong, T.-D. Hoang, M.A. Wahab, K. Hackl, H. Nguyen-Xuan, A new thermoelastic model for agglomerated and randomly-oriented CNT-reinforced bio-inspired materials: Temperature-dependent free vibration analysis of FG-CNTR-TPMS plates, Engineering Analysis with Boundary Elements 174 (May 2025) 106157, https://doi.org/10.1016/j.enganabound.2025.106157.
[59] E. Kaartinen, K. Dunphy, A. Sadhu, LiDAR-Based Structural Health monitoring: applications in Civil Infrastructure Systems, Sensors 22 (12) (Jan. 2022) 4610, https://doi.org/10.3390/s22124610.